

Biomedical Materials



PAPER

Acoustic and mechanical characterization of 3D-printed scaffolds for tissue engineering applications

RECEIVED
10 May 2018

REVISED
12 July 2018

ACCEPTED FOR PUBLICATION
18 July 2018

PUBLISHED
6 August 2018

Mitra Aliabouzar , Grace Lijie Zhang  and Kausik Sarkar 

Department of Mechanical and Aerospace Engineering, The George Washington University, Washington DC 20052, United States of America

E-mail: sarkar@gwu.edu

Keywords: acoustic characterization, attenuation coefficient, hydrogel scaffolds, 3D printing, acoustic impedance, mechanical characterization, proliferation

Abstract

The acoustic and mechanical properties of 3D-printed porous poly-(ethylene glycol)-diacrylate (PEGDA) hydrogel scaffolds were investigated using an ultrasound pulse echo technique on different scaffold microstructures (solid, hexagonal and square pores). Acoustic parameters such as speed of sound, acoustic impedance and attenuation coefficient as well as physical parameters such as the pore structure, effective density and elastic moduli were determined. The results show that microstructure (porosity and pore geometry) plays a crucial role in defining properties of 3D-printed scaffolds, achieving the highest attenuation for the scaffold with hexagonal pores and showing a decrease in sound speed and elastic moduli with increasing porosity. The properties were also found to be similar to those of soft tissues, making PEGDA scaffolds a suitable candidate for tissue engineering applications. To evaluate their cellular performance, adhesion and proliferation of human mesenchymal stem cells (hMSCs) in these scaffolds were investigated. The porous scaffolds performed better than the solid one, recording the highest cell attachment and growth for the scaffold with the square pores.

1. Introduction

Tissue engineering has recently emerged as an important technology with promises to replace, repair and regenerate human tissues. One of its key components is the design and development of effective three-dimensional (3D) tissue scaffolds that can provide a suitable microenvironment mimicking the *in vivo* situation. An ideal tissue engineering scaffold should be biocompatible, have suitable porosity to allow cell migration as well as nutrient exchange and appropriate mechanical properties [1, 2]. For better integration of 3D scaffolds and the host tissue, accurate characterization of scaffolds is crucial. Here, we report an acoustic and mechanical characterization—speed and attenuation of ultrasound as well as elastic moduli—of various 3D-printed tissue engineering scaffolds and investigate their properties and suitability.

Conventional methods for scaffold fabrication such as solvent casting, gas foaming, and particulate and porogen leaching have major drawbacks including the use of toxic solvents, inability to create precise

pore size and geometry, long manufacturing periods and low reproducibility [3, 4]. 3D printing, on the other hand, offers great advantages such as quick fabrication, incorporation of different materials as well as micro- and nanoparticles, and finally high precision and accuracy on thickness, porosity, pore size as well as geometry so that they closely resemble the target tissue [5–8].

Understanding the properties of 3D-printed scaffolds is critical for facilitating their proper modeling and efficient design. Surface topography, chemistry as well as mechanical properties have been shown to significantly influence scaffolds' biological functionalities including cell adhesion, proliferation and differentiation [9–11]. Each method of characterization has its own advantages and disadvantages and often they complement rather than replace each other. Conventional means of classical mechanical characterization of tissue engineering scaffolds, often require destructive testing or means that can compromise the sterility of the samples [12]. In contrast, ultrasonic techniques offer a cost-effective, non-invasive and

non-destructive characterization without lengthy prior preparation [13, 14]. Furthermore, it can directly probe the elastic and viscous properties of a material by measuring the speed of ultrasound and its attenuation. Such acoustic characterization has been performed for biological tissues [15–17] as well as a number of synthetic polymeric constructs made of PLGA [18], Silicone [19], Polyvinyl alcohol [15], Agar gel [19] and polyacrylamide gel [20] for their possible use as human tissue substitutes. However, all these studies were conducted on thin slabs of solid hydrogel samples which do not truly represent the highly porous body environment. A few studies that have investigated the role of microstructure such as porosity and pore size on ultrasonic properties of bone mimicking phantoms [21–24] focused on biomaterials fabricated by conventional techniques and therefore suffered from irregular surface patterns with no control over pore size and porosity. On the other hand, the ultrasonic properties of 3D-printed scaffolds with custom designed microstructures have not been measured before.

In this work, we use polyethylene (glycol) diacrylate (PEGDA) bioink to develop 3D-porous scaffolds. PEGDA has been widely used in biomedical applications including tissue engineering, wound healing and drug delivery due to its high water content, biocompatibility and easy printability [6]. Using an in-house built table-top stereolithography based 3D printer in our lab, we are able to 3D print tissue scaffolds from a variety of biomaterials with varying inner pore and channel structures to closely customize the geometry and microenvironment of a patient's defect site [5, 25–27]. Acoustic properties of 3D-printed micro-structured PEGDA scaffolds have not been investigated before.

We measure ultrasound attenuation coefficient, speed of sound and acoustic impedance as well as mechanical properties of PEGDA scaffolds with varying thicknesses and pore geometries, and compare the results with properties of biological tissues. In addition, we investigate whether and how porosity and pore geometry can affect human mesenchymal stem cells (hMSCs) attachment and proliferation on these scaffolds. In recent years, tissue engineering approach has focused on hMSCs as an important cell source because of their ability to differentiate into various cell types [28–30].

2. Materials and methods

2.1. Hydrogel scaffold fabrication

An in-house built tabletop stereolithography-based 3D printer was used to fabricate structured hydrogel scaffolds (figure 1(a)). The printer consists of a movable stage, which is capable of 3D axial movement and is equipped with a UV (355 nm) laser source (MarketTech, Scotts Valley, CA). The printing

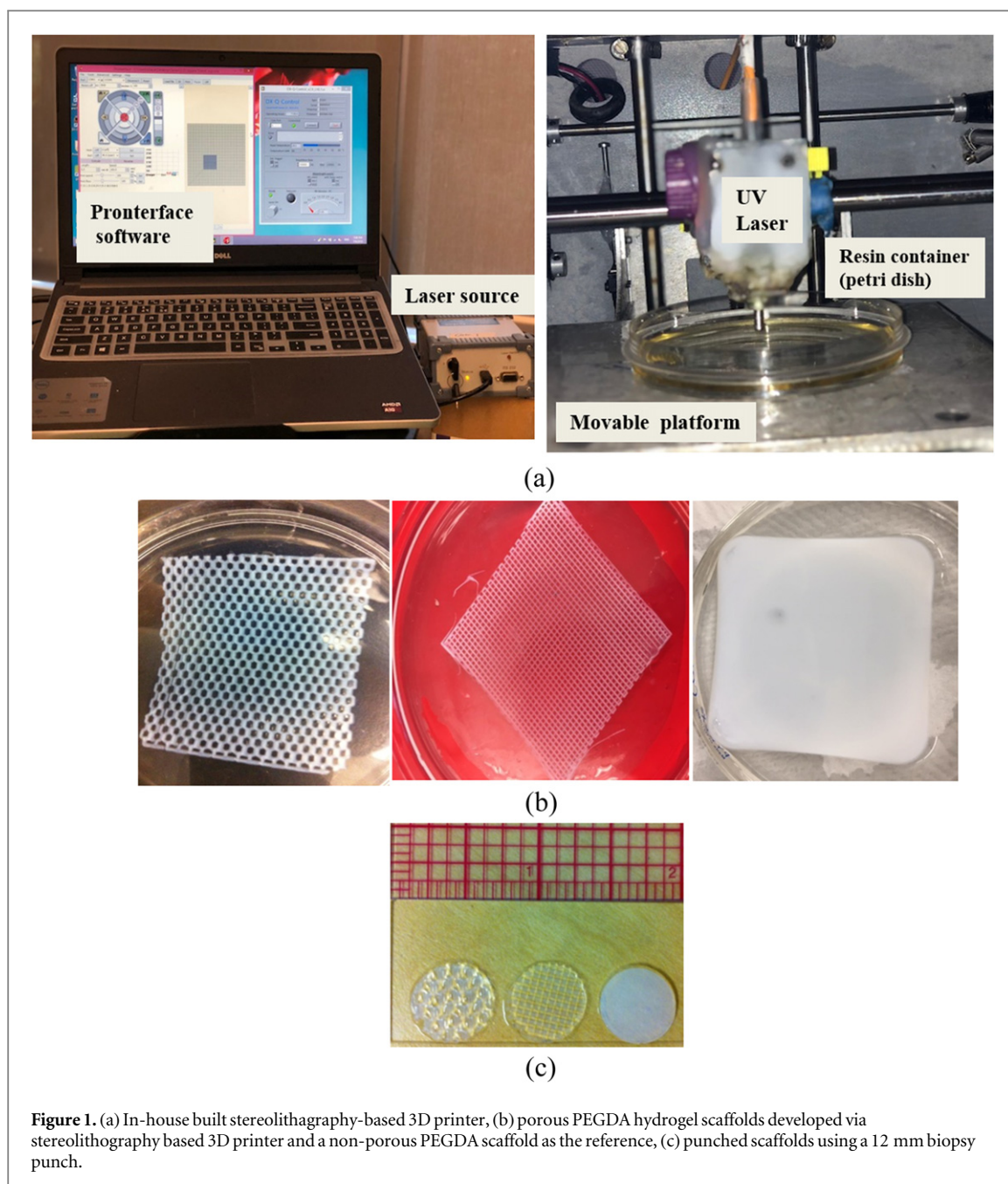
configuration is controlled by an open source software (Pronterface) package. 3D constructs were first created using computer aided design (CAD) software. Afterwards, the geometric models were exported into Slic3r software to program the porosity (infill density) and pore geometry. Once completed, the corresponding STL file was sent to the 3D printer. The print speed was maintained at 25 mm s^{-1} and the frequency of pulsed signal used to print the structured patterns varied from 8 to 11 kHz. Using this 3D printer, we were able to create 3D-porous scaffolds with hexagonal and square pore geometries. Additional details about stereolithography printing can be found elsewhere [5–7].

Hydrogel resins were prepared by mixing 40 wt% poly (ethylene glycol) (PEG, Mn 300) and 60 wt% poly (ethylene glycol) diacrylate (PEG-DA, Mn 575) in the presence of a photo initiator, Bis(2, 4, 6-trimethylbenzoyl)-phenylphosphineoxide (BASF, Florham Park, NJ) (0.5 wt% of PEGDA), in a 50 ml centrifuge tube. To ensure homogenous mixing and adequate dissolution, the tube was left to rest overnight on a shaker. For printing a single layer, 3 ml of the hydrogel resin was pipetted into a 10 cm diameter glass petri dish and placed upon the print bed. It was then cured by laser directed by the CAD file to produce an effective layer of $400 \mu\text{m}$. This process was then repeated for each layer starting with fresh deposition of resin solution and allowing it to spread over the previous layer. Three $400 \mu\text{m}$ thick layers were printed for the PEGDA scaffolds. Once the printing was complete, the cured scaffolds were rinsed with acetone and then distilled water to remove unreacted resin.

For acoustic studies, scaffold blocks of dimension $50 \times 50 \times 1.2 \text{ mm}^3$ with different pore geometries were 3D-printed (figure 1(b)). The thickness of the scaffolds was determined using a digital caliper having a resolution of 0.01 mm. One solid sample of the same dimension and material was cured via ultraviolet (UV) exposure and used as the reference. Since manufacturing and processing conditions strongly influence the results, all the samples were prepared on the same day with fresh resins and allowed to swell in ultrapure water overnight prior to acoustic measurements. For the cellular evaluation, these constructs were punched into uniform cylindrical scaffolds using a 12 mm biopsy punch (figure 1(c)).

2.2. Ultrasonic testing

A pulse echo technique was used to determine both sound propagation speed and attenuation coefficient of 3D-printed hydrogel scaffolds. The schematic diagram of the experimental setup is shown in figure 2. In this configuration, a single piezoelectric transducer acts both as a transmitter and a receiver of the sound wave. The transducer is driven by a commercially available pulser-receiver (model 5800; Panametrics-NDT, Waltham, MA), which produces short pulses with a pulse repetition frequency of 100 Hz. The



received signal is then sampled using a digital oscilloscope (Model TDS 2012; Tektronix, Beaverton, OR). Each measurement was averaged 64 times to increase the signal-to-noise ratio. This digitizer was linked to a personal computer where the data were transferred for further processing. The recorded signals were then analyzed using a fast Fourier transform (FFT) program developed in-house written in MATLAB.

The measurements were carried out in a polycarbonate water tank (50 mm × 50 mm × 45 mm) at room temperature (20 °C). The samples were subjected to ultrasound from above at a normal incidence using degassed deionized (DI) water as a coupling fluid. Care was taken to make sure that the sample surface immersed in water was completely flat with respect to the incoming wave to avoid unwanted

scattering. To obtain the acoustic attenuation and speed of sound in a frequency range from 1 to 12 MHz, three unfocused immersion transducers (Olympus NDT, Waltham, MA) with central frequencies of 2.25 (V306, -6 dB: 1.57–3.05 MHz), 5 (V309, -6 dB: 2.25–7.8 MHz) and 10 MHz (V311, -6 dB: 6.44–12.9) with an element diameter of 0.5 inch were used. The transducers were calibrated using a capsule hydrophone (HGL-0200, ONDA, Sunnyvale, CA) in a water tank filled with degassed DI water. The acoustic wavelengths studied here (150–700 μm) are smaller than the thickness of the samples, ensuring that our acoustic measurements probe the bulk properties. Note that the samples positioned at 40 mm from the surface of the transducer are in the near field ($N = 60$ mm at 2.25 MHz, 132 mm at 5 MHz and 266 mm at

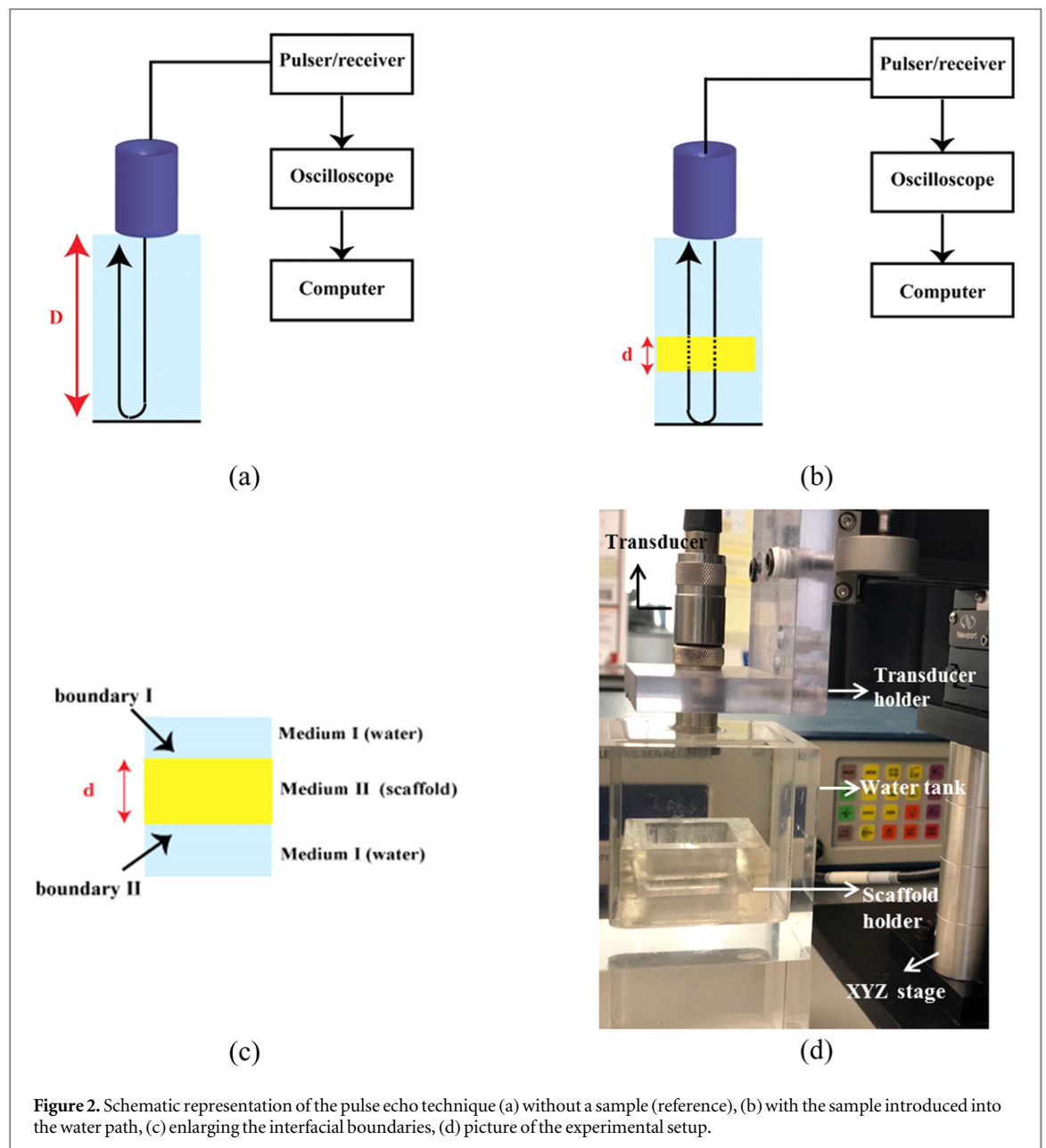


Figure 2. Schematic representation of the pulse echo technique (a) without a sample (reference), (b) with the sample introduced into the water path, (c) enlarging the interfacial boundaries, (d) picture of the experimental setup.

10 MHz). However, experiments repeated with a recently acquired 10 MHz transducer with a smaller element diameter 0.25 inch ($N = 66$ mm) produced no significant variation validating the experimental procedure.

For each reading we acquired fifty voltage–time RF traces in an averaged mode and stored for further processing. Each measurement is averaged over 8 readings per sample, repositioning the sample after each reading. This is repeated three times on three freshly printed samples.

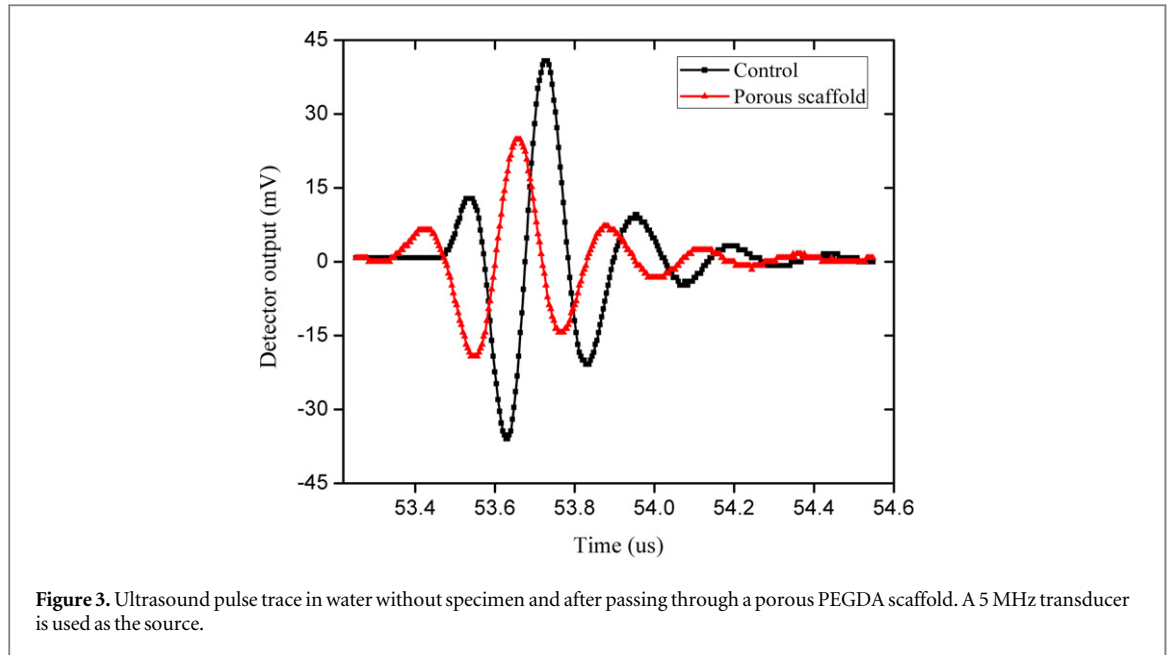
2.3. Density and porosity measurements

For density and porosity measurements, scaffolds were punched out using a 12 mm biopsy punch as shown in figure 1(c). Punched scaffolds were dried overnight and weighed in order to calculate their apparent mass density ρ_{app} using the initial volume (measured

thickness of 1.2 mm and diameter of 12 mm using a digital caliper with sensitivity of 0.01 mm), as drying did not cause any significant change in the sample volume. The sample specific porosity ϕ is then determined as [31, 32]

$$\phi = (1 - \rho_{app}/\rho_s), \quad (1)$$

where ρ_s is the solid phase density of the dried reference (non-porous) scaffold. To calculate their densities in wet state, all scaffolds were soaked in DI water and weighed after 24 h. The density of the scaffolds was calculated from the ratio of the apparent masses in air and water and knowledge of the density of water at room temperature. For the porous scaffolds, the density of a given saturated material is related to the densities of the frame as well as the saturating fluid, and hence it can be written as follows [14]:



$$\rho_p = (1 - \phi)\rho_s + \phi\rho_w, \quad (2)$$

where ρ_p is the density of porous scaffold, ρ_s density of the skeletal frame in the wet state (PEGDA non-porous scaffold) and ρ_w is the water density. All the measurements were repeated 6 times from different positions of the printed scaffolds and averages were computed.

2.4. Speed of sound and attenuation coefficient measurements

Both the speed of sound and attenuation measurements were carried out in the same experimental setup shown in figure 2(d). We used a time-of-flight approach; the temporal shift (Δt) between the pulse transit times with and without the scaffolds in the path- to determine sound velocities in the scaffolds. Knowing the speed of sound in water and the sample thickness, the velocity of sound in the specimen is [19, 33, 34]

$$C_s = \left(\frac{1}{C_w} - \frac{\Delta t}{2d} \right)^{-1}, \quad (3)$$

where C_s and C_w are the speeds of sound in the scaffold and water, respectively and d is the sample thickness. The values were computed by averaging over six measurements. The speed of sound in water was taken to be 1483 m s^{-1} [22, 35]. This value was used in all subsequent speed of sound calculations. A typical voltage–time signal with and without the porous scaffolds is shown in figure 3.

To measure the attenuation of the sound traveling through the sample, we compute the FFT of the signal obtained in the pulse echo mode. For the signal transmitted through water alone (figure 2(a))

$$A_w(f) = U_0(f)e^{-2\alpha_w(f)D}, \quad (4)$$

where $\alpha_w(f)$ is the attenuation coefficient of water, D is the water path length and $U_0(f)$ in the initial amplitude and $A_w(f)$ is the FFT of the received signal

amplitude. Referring to figure 2(b), for propagation through a sample:

$$A_s(f) = U_0(f)e^{-2\alpha_w(f)(D-d)} (T_{I,II} T_{II,I})^2 e^{-2\alpha_s(f)d},$$

$$T_{I,II} = \frac{2Z_{II}}{Z_I + Z_{II}}, \quad T_{II,I} = \frac{2Z_I}{Z_I + Z_{II}} \quad (5)$$

where $A_s(f)$ is the FFT of the received signal amplitude, d is the sample thickness, $\alpha_s(f)$ is the attenuation coefficient of the sample, $T_{I,II}$ is the transmission coefficient at boundary I (between water and tissue) and $T_{II,I}$ is the transmission coefficient at boundary II (between tissue and water) (figure 2(c)). Z_I and Z_{II} are the characteristic acoustic impedances (product of the density and the speed of sound) of water and scaffold material. From (4) and (5), one finds

$$\alpha_s(f) - \alpha_w(f) = \left[\frac{1}{2d} \ln[A_w(f)/A_s(f)] + \frac{1}{d} \ln(T_{I,II} T_{II,I}) \right]. \quad (6)$$

We use equation (6) to measure the attenuation knowing the transmission coefficients $T_{I,II}$ and $T_{II,I}$ for all the scaffolds. To validate the accuracy of our methodology we measured attenuation using the same scaffold with two different thicknesses to eliminate the transmission coefficient calculations. Both techniques resulted in similar values (data not shown).

Please note that in order to determine density, porosity, speed of sound and other acoustic properties, the porous scaffold material with an inherently heterogeneous structure has been treated as a coarse grained homogeneous continuum. In effect these quantities are indicative of the bulk system averaging over the variations in the scale of the pore dimension. For the acoustic propagation the underlying analysis is a gross approximation as it is strictly valid only for

wavelength far larger compared to the pore dimension. To accurately solve the acoustic propagation through the porous geometry one needs to satisfy the boundary condition on the actual pore surface using e.g. a finite element method (FEM). The present method is sufficient for our purpose of gross characterization of the sample. Also note that the same acoustic attenuation value experimentally computed from measurements in samples of different thicknesses (figure 5) partially validates the homogenized treatment.

2.5. SEM analysis and mechanical testing

A scanning electron microscope (SEM, Zeiss NVision 40FIB) was employed to assess the matrix morphology and pore structure at 2 kV accelerating voltage. To make the samples conductive for SEM imaging, they were coated with gold nanoparticles using a standard argon gas sputter-coater set to 15 mA.

The compressive elastic modulus of the scaffolds was determined via uniaxial compression testing ($n = 6$) (Applied Test Systems, Butler, PA) fitted with a 100 N load cell at a crosshead speed of 0.5 mm min^{-1} . Samples were punched by a 12 mm biopsy punch and were placed in ultrapure water overnight prior to testing. We plotted the stress-strain curves and calculated the Young's modulus from the linear region.

2.6. Cell culture, adhesion and proliferation in 3D-printed hydrogel scaffolds

hMSCs were obtained from the Texas A&M Health Science Center, Institute for Regenerative Medicine. The cells (passage #3-6) were cultured in complete media composed of Alpha Minimum Essential medium (α -MEM, Gibco, Grand Island, NY) supplemented with 16% fetal bovine serum (Atlanta Biologicals, Lawrenceville, GA), 1% L-glutamine (Invitrogen, Carlsbad, CA) and 1% penicillin:streptomycin (Invitrogen, Carlsbad, CA) and incubated under standard cell culture conditions (37°C , a humidified, 5% $\text{CO}_2/95\%$ air environment). Prior to cell seeding, the samples were sterilized via exposure to ultraviolet light for 15 min, flipped and exposed for another 15 min, and then rinsed with PBS three times. Subsequently, the sterilized samples were incubated with culture media described above for 24 h before cell seeding. Porous multilayer scaffolds of different geometries were evaluated for hMSC adhesion. For adhesion studies, all samples were seeded at a density of 25×10^3 cells per scaffold in 24-well plates. For 5 day proliferation studies, a cell density of 5×10^3 was used and incubated for 1, 3 and 5 days. After the prescribed time periods, the scaffolds were rinsed using PBS to remove non-adherent cells.

The cell proliferation on each scaffold was quantified via MTS assay (CellTiter 96 Aqueous Non-Radioactive Cell Proliferation, Promega, Madison, WI) and

analyzed using a Thermo Scientific Multiskan GO spectrophotometer at a setting of 490 nm wavelength [7].

2.7. Statistical analysis

All cell studies were run in triplicates. And then they were repeated three times on different days to further allow for day-to-day and donor variations leading to $n = 9$. Data are presented as the mean \pm standard error of the mean unless indicated otherwise. These statistical analyses were conducted using Student's t-test. Statistical significance was considered at $p < 0.05$.

3. Results and discussion

3.1. Morphological characterization of 3D-printed scaffolds

The microstructure and morphological features of the pores were examined using a scanning electron microscope (SEM, Zeiss NVision 40FIB). SEM images of 3D-printed scaffolds with square and hexagonal pore shapes are displayed in figures 4(b) and (c). 3D-printed hydrogel scaffolds are highly porous with open and interconnected pores that are surrounded by polymer walls. As shown in the figure, the pores and channels in the 3D-printed scaffolds are distinct and have corresponded well to the pre-designed shapes (figure 4(a)). The square pattern is created by printing lines in alternate direction, which contributed to the shadows in the SEM image in figure 4(c). Using image J software (imagej.nih.gov), the SEM micrographs were further processed to determine the average size of the pores and the surrounding walls (table 1). Note that pores increased the available substrate surface area by 700% for scaffolds with square pores and 350% for those with hexagonal pores. Table 1 summarizes the physical properties of the 3D-printed scaffolds. The wet density of PEGDA computed here matches with the literature (as well as manufacturer provided value of 1.12 g cm^{-3}). It is also close to the values for soft tissues such as breast (1.06 g cm^{-3}), liver (1.07 g cm^{-3}), wet tendon (1.11 g cm^{-3}), and human skin (1.19 g cm^{-3}) [36].

3.2. Ultrasonic attenuation

The attenuation coefficient was determined for the non-porous scaffold and scaffold with square pores with varying thicknesses using a transducer with a central frequency of 10 MHz. Figure 5 shows that the acoustic attenuation coefficients averaged over the -6 dB transducer bandwidth remain almost constant (as it should be for a material parameter validating our methodology) with values of 1.39 ± 0.16 and $2.44 \pm 0.05 \text{ Np cm}^{-1}$ for solid and square scaffolds respectively.

Figure 6(a) plots the power spectrum of the transmitted signals obtained by a 10 MHz transducer

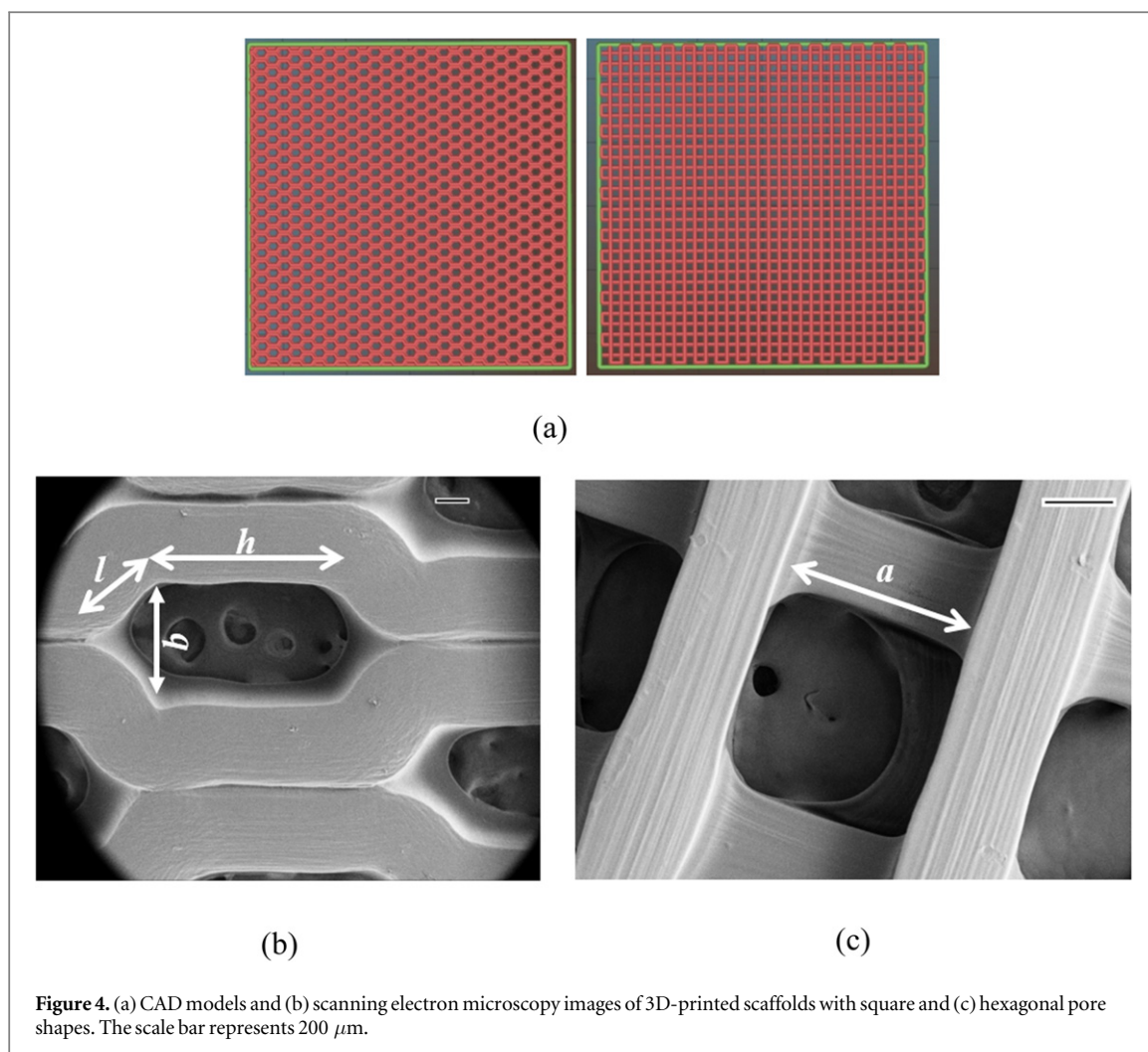


Figure 4. (a) CAD models and (b) scanning electron microscopy images of 3D-printed scaffolds with square and (c) hexagonal pore shapes. The scale bar represents $200\ \mu\text{m}$.

as a function of frequency for the three different scaffolds—solid, hexagonal pores and square pores. It shows that the attenuation is highest for the scaffold with hexagonal pores. Figure 6(b) shows attenuation for all three samples as a function of frequency. The data obtained by transducers with three different central frequencies have been collated here. The average attenuation coefficients for solid, hexagonal and square scaffolds measured using transducers with different central frequencies of 2.25, 5 and 10 MHz are presented in table 2.

From figure 6(b), one notes that aggregate attenuation collated from all three different transducers is significantly higher for the scaffold with hexagonal pores compared to the other two possibly due to the higher scattering cross-section—pore dimensions are comparable to the incident wavelength making scattering an important phenomenon—from the asymmetric hexagonal pores [37]. The average aspect ratio of hexagonal pores is ~ 1.8 compared to ~ 1.01 for the square pores. Jeong and Hsu [38] reported a higher attenuation coefficient for asymmetrical and longer pores compared to the spherical ones. The lower attenuation coefficient for non-porous scaffolds may be attributed

to the flat nature of the surface and therefore much less likely to contribute to surface scattering and diffraction [23], and such a behavior has also been observed in carbon composites as well as graphite/epoxy composites [23, 24, 39]. Attenuation increases with frequency for the solid scaffold and the one with square pores for all frequencies. However, for the scaffold with hexagonal pores, attenuation shows a peak value around 9 MHz. Such a non-monotonous behavior has also been seen from scatterers with increasing asymmetry [37].

The approximate linear increase of attenuation with frequency for the PEGDA scaffolds in the range of 1.5–10 MHz, (figure 6(b)) has been fitted to obtain slopes $d\alpha/df$ ($\text{Np cm}^{-1} \text{MHz}^{-1}$) of 0.71 ($r^2 = 0.94$), 0.33 ($r^2 = 0.89$) and 0.17 ($r^2 = 0.91$) for hexagonal, square and solid scaffolds, respectively. Such a linear variation with frequency has also been noted for soft tissues over a broad frequency range from 1 to 50 MHz [40–42]. The attenuation values recorded in table 2 for PEGDA scaffolds fall within the range of reported values for the soft tissues $-3.5\ \text{Np cm}^{-1}$ for human lung at 1 MHz, $2.19\ \text{Np cm}^{-1}$ for human cartilage at 5 MHz and $0.4\ \text{Np cm}^{-1}$ at 1 MHz for human skin [36, 43].

Table 1. Measured properties of 3D-printed scaffolds: geometry (symbols defined in figure 4), density and porosity.

| Scaffold | Pore size (μm) | Pore interconnecting wall (μm) | Volume (mm^3) | Dry mass (mg) | ρ_s (g cm^{-3}) | ρ_{app} (g cm^{-3}) | \emptyset (%) | ρ_{wet} (g cm^{-3}) |
|----------|---|---|--------------------------|---------------|---------------------------------|--|-----------------|--|
| Solid | — | — | 135.64 | 44.4 | 0.3273 | 0.3273 | — | 1.06 ± 0.01 |
| Hexagon | $l = 548.6 \pm 26, h = 1062.6 \pm 60, b = 768.3 \pm 31$ | 1038 ± 21 | 135.64 | 30.6 | 0.3273 | 0.2255 | 33 | 1.04 |
| Square | $a = 580 \pm 18$ | 265.7 ± 17 | 135.64 | 22 | 0.3273 | 0.1669 | 47 | 1.03 |

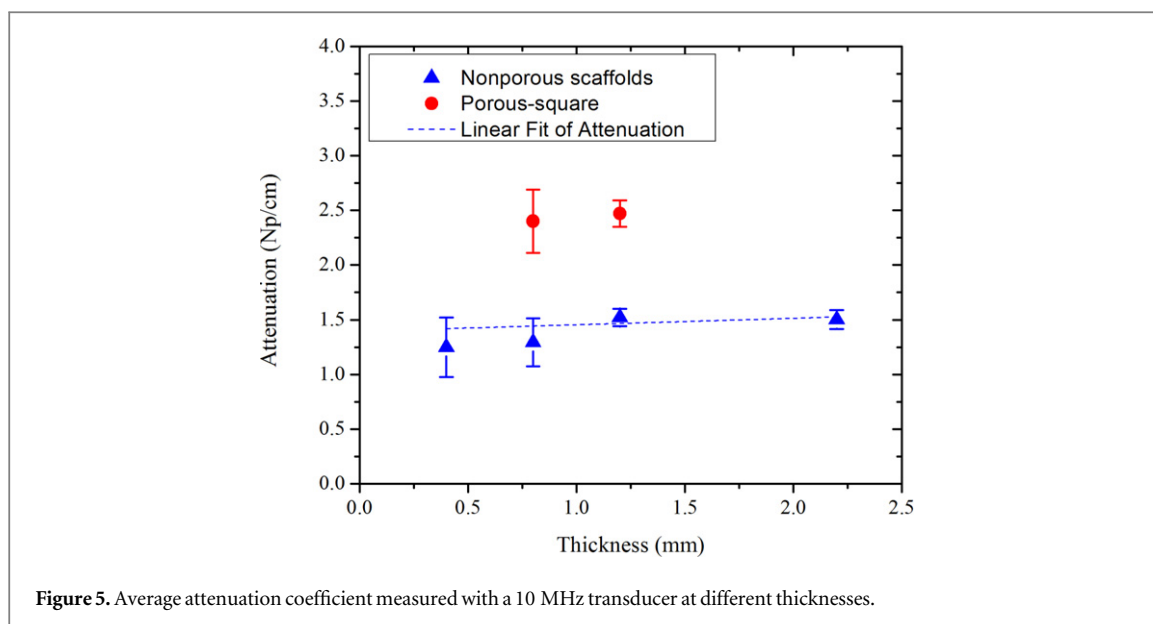


Figure 5. Average attenuation coefficient measured with a 10 MHz transducer at different thicknesses.

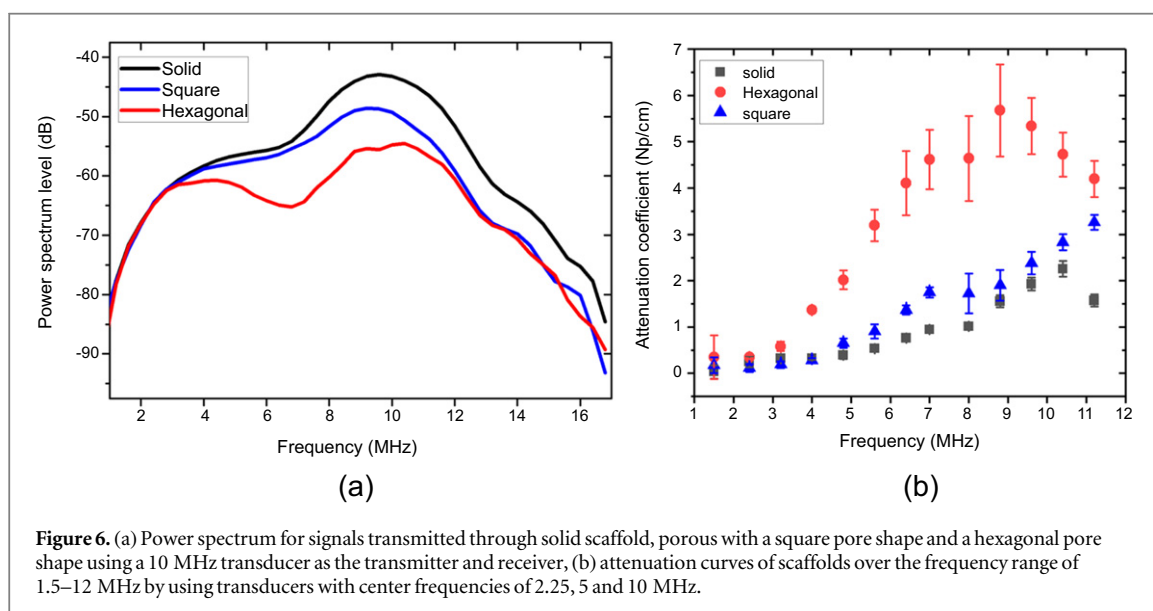


Figure 6. (a) Power spectrum for signals transmitted through solid scaffold, porous with a square pore shape and a hexagonal pore shape using a 10 MHz transducer as the transmitter and receiver, (b) attenuation curves of scaffolds over the frequency range of 1.5–12 MHz by using transducers with center frequencies of 2.25, 5 and 10 MHz.

3.3. Sound velocity

We measured the speed of sound for all the samples at 2.25, 5 and 10 MHz according to equation (3). We found that speed of sound remained constant for all the scaffolds with increasing frequency (figure 7 (a)). Previous studies on soft tissues have also shown very little dispersion in the range of 1–15 MHz [36]. Figure 7(b) indicates that the speed of sound decreases from solid scaffold, with increasing porosity achieving a value close to speed of sound in water for the square scaffold (47% porosity). The decrease is due to a decrease in the effective elastic stiffness of the scaffolds with increasing porosity (determined by mechanical testing and recorded in figure 8). The values of the speed of sound computed here for PEGDA scaffolds (also listed in table 2) are close to those found in biological soft tissues such as in kidney (1558–1568 m s^{-1}), liver (1550–1607 m s^{-1}), cardiac muscle ($\sim 1529 \text{ m s}^{-1}$), articular cartilage (1500–1700 m s^{-1}), human breast

tissue (1430–1570 m s^{-1}) and human skin (1540 m s^{-1}) [36, 44, 45]. Note that the standard deviation in the computed value for the solid scaffold is slightly larger than the other two, but still quite small $\sim 0.65\%$. With the knowledge of speed of sound and density their product, the characteristic acoustic impedance, was calculated and summarized in table 2. The obtained value of characteristic acoustic impedance for the non-porous PEGDA sample is similar to what has been published by Demitri, *et al* [46] for a hydrogel mixture of PEGDA and water.

3.4. Bulk and Young's moduli of scaffolds

We compute the effective bulk elastic modulus of the scaffolds using the relation

$$K = \rho C^2, \quad (7)$$

where ρ is the density of the material and C is the longitudinal velocity of ultrasound waves in the

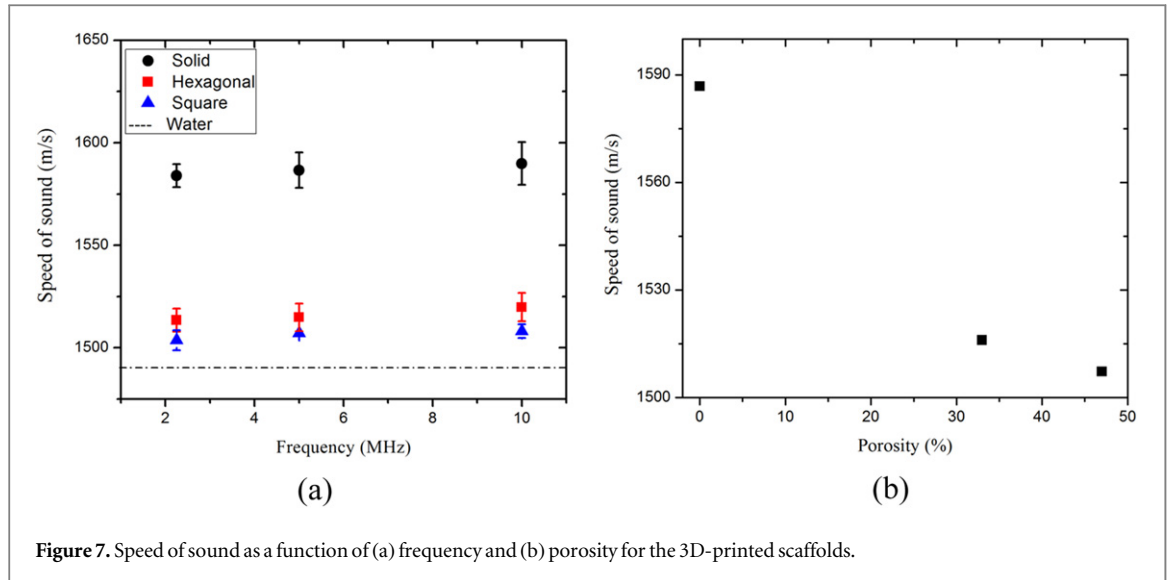


Figure 7. Speed of sound as a function of (a) frequency and (b) porosity for the 3D-printed scaffolds.

Table 2. Averaged attenuation coefficients (using different frequency transducers), sound speed, acoustic impedance, elastic moduli and Poisson's ratio of PEGDA scaffolds.

| 3D-printed scaffolds | Attenuation coefficient (Np cm^{-1}) | | | Speed of sound (m s^{-1}) | Characteristic impedance ($10^6 \text{ Kg m}^{-2} \text{ s}^{-1}$) | Young's modulus (MPa) | Bulk's modulus (GPa) | Poisson's ratio |
|----------------------|---|-----------------|-----------------|--------------------------------------|--|-----------------------|----------------------|-----------------|
| | 2.25 MHz | 5 MHz | 10 MHz | | | | | |
| Hexagonal pore | 0.34 ± 0.11 | 2.18 ± 1.09 | 4.68 ± 0.6 | 1519 ± 2.1 | 1.58 | 1.01 ± 0.18 | 3 | 0.499 92 |
| Square pore | 0.15 ± 0.04 | 0.84 ± 0.45 | 2.44 ± 0.69 | 1508 ± 3.2 | 1.55 | 0.42 ± 0.15 | 2.7 | 0.4996 |
| Solid | 0.14 ± 0.08 | 0.49 ± 0.2 | 1.47 ± 0.58 | 1589 ± 10.42 | 1.7 | 1.78 ± 0.4 | 3.5 | 0.4999 |

medium [47]. The bulk elastic moduli are computed to be 3.5, 3 and 2.7 GPa for the solid, hexagonal and square samples, respectively (also listed in table 2). Note that water at 22 °C has a bulk modulus of 2.24 GPa.

In order to obtain Young's modulus values for the porous and non-porous hydrogel scaffolds, we performed unidirectional compression test and plotted the stress–strain curves (figure 8(a)). Stress (MPa) was calculated as the force divided by the apparent cross-sectional area of the scaffold while strain (mm mm^{-1}) was the ratio of the displacement over the initial thickness. As noted before, this analysis is premised on treating the highly anisotropic and heterogeneous porous material as an effective homogeneous medium. Especially for the scaffold with square pores, due to their construction of printed lines in alternate directions, the compressive stress is disproportionately transferred through the corners, where the fibers in different layers cross (see figure 4(c)), as was shown by FEM solution [48]. The solid scaffold shows the steepest slope followed by porous scaffolds with hexagonal and square pores (figure 8(a)). Young's modulus is computed from the linear region of the curves. Figure 8(b) shows that the averaged Young's modulus

decreases with porosity, recording the highest value (1.9 MPa) for the non-porous hydrogel scaffold, as expected [49]. There we also plot a theoretical estimate of the Young's modulus as a function of porosity [50]:

$$E_p = E_s(1 - \Phi)^3, \quad (8)$$

where E_s and E_p are the Young's moduli of the solid (measured directly) and porous scaffolds, respectively. The measured moduli for the porous scaffolds compare reasonably with the theoretical estimates, partially validating the effective homogenized theory analysis used here. Computed moduli for the PEGDA scaffolds are similar to the ones reported by De Santis *et al* [51] and also lie within the range reported for biological tissues such as cartilage (0.75–1 MPa). Knowing the bulk and Young's moduli, one can determine Poisson's ratio according to

$$\nu = \frac{3K - E}{6K}. \quad (9)$$

The values of K and E listed in table 2 are used to compute ν (also listed in table 2), which achieves a value of 0.5 characteristic of an incompressible material.

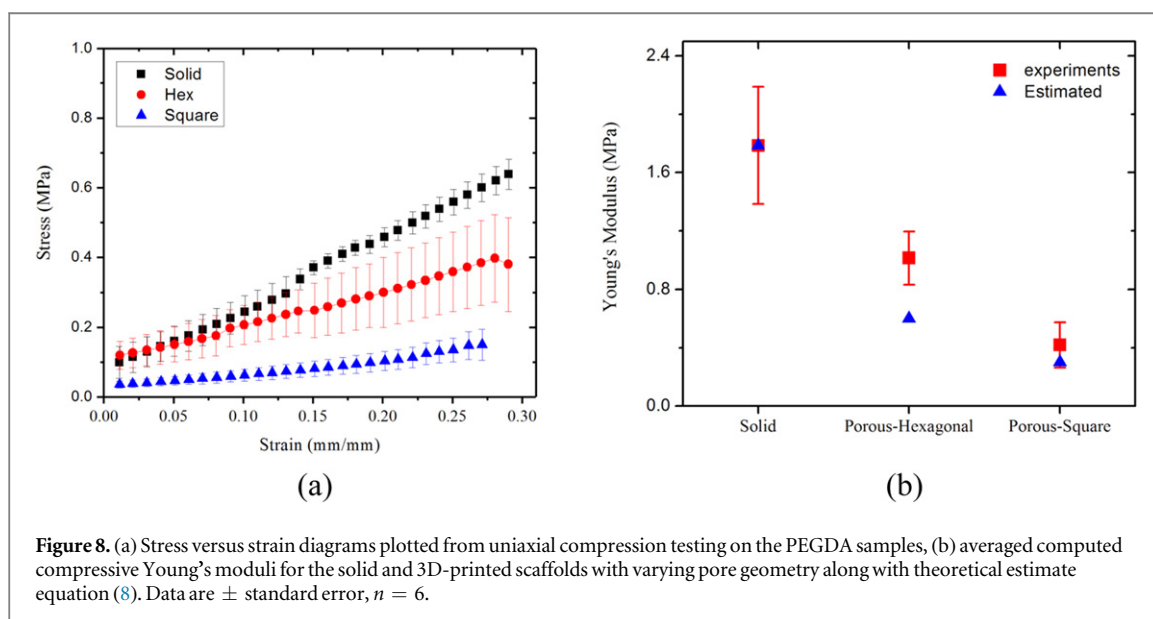


Figure 8. (a) Stress versus strain diagrams plotted from uniaxial compression testing on the PEGDA samples, (b) averaged computed compressive Young's moduli for the solid and 3D-printed scaffolds with varying pore geometry along with theoretical estimate equation (8). Data are \pm standard error, $n = 6$.

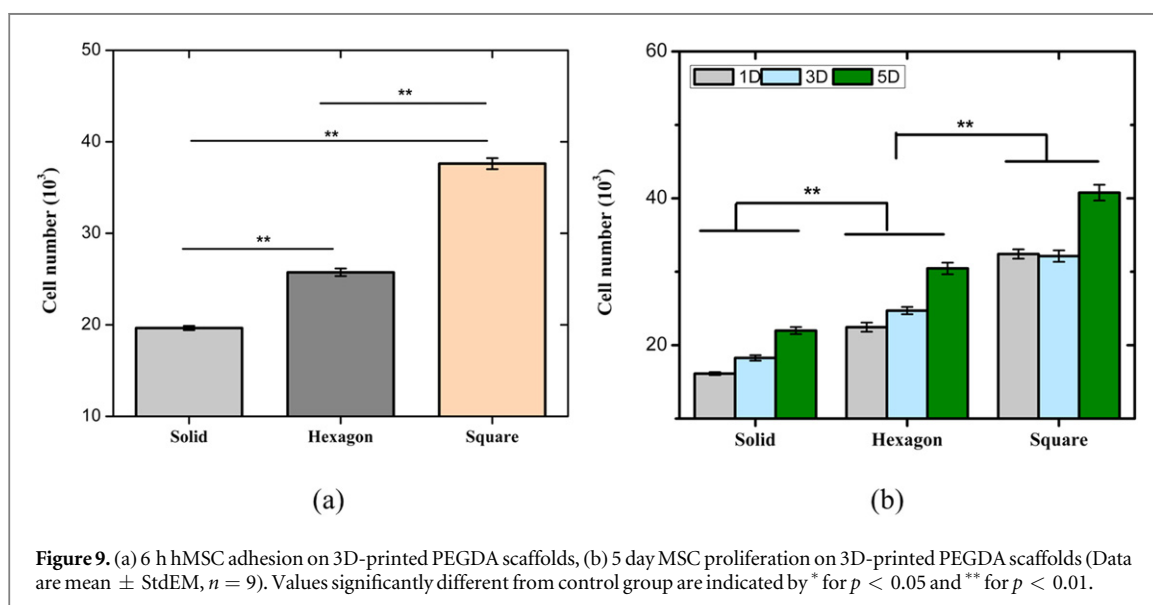


Figure 9. (a) 6 h hMSC adhesion on 3D-printed PEGDA scaffolds, (b) 5 day MSC proliferation on 3D-printed PEGDA scaffolds (Data are mean \pm StdEM, $n = 9$). Values significantly different from control group are indicated by * for $p < 0.05$ and ** for $p < 0.01$.

3.5. Effect of pore geometry on hMSC adhesion and proliferation

Figure 9 shows hMSC adhesion after 6 h and 5 day proliferation in different PEGDA scaffolds. The data indicate that hMSCs expectedly grow better on porous PEGDA scaffolds compared to the solid one since porous scaffolds provide a suitable environment for cells to grow and facilitate nutrient and oxygen diffusion as well as waste removal [52]. Scaffolds with square pores exhibited significantly higher adhesion and proliferation compared to the hexagonal one (46% higher after a 6 h adhesion study) which is in agreement with the previous studies [25, 27]. Previously, we have confirmed cell growth and spreading on the 3D-printed porous scaffolds using optical and confocal microscopies [25, 27]. Availability of increased surface area for the cells to adhere in porous

scaffolds clearly is one of the key factors for the results observed here. The higher proliferation in scaffolds with square channels at least partially can be attributed to its higher porosity—47% compared to 33% for that with hexagonal pores—and therefore its higher surface area. However, we have found in a previous study that a scaffold with square pores (64% porous) led to a higher cell proliferation than a scaffold with hexagonal pores (78% porous) [25]. Moreover, recently a curvature driven effect has been suggested claiming better adhesion and spreading of hMSCs to corners with larger curvatures [53–56], which might also have led to better results in square pores. Nelson, *et al* correlated the curvature driven growth to regions of higher force concentrations [57]. Firmer understanding of the effect of geometrical features of the tissue scaffolds such as pore geometry and porosity is critical for

optimized scaffold design. One would need systematic studies varying pore anisotropy at a constant porosity.

4. Conclusion

In this study, for the first time, ultrasonic characterization of 3D-printed porous scaffolds for tissue engineering applications has been performed. Scaffolds have been designed and fabricated using a stereolithography based 3D printing technique, which corresponded well with the original CAD models developed in-house. We measured attenuation coefficient, sound speed, acoustic impedance, density, and bulk and Young's moduli, varying pore geometry and thereby scaffold porosity. The properties computed were found to be similar to those of biological tissues. Although most of the properties could be explained by relating them to the porosity—sound speed, bulk and Young's moduli decreasing with increasing porosity—we found that pore asymmetry too plays an important role in determining attenuation; enhanced asymmetry of hexagonal pores led to a higher attenuation of ultrasound compared to non-porous scaffold as well as one with higher porosity but with square pores. To evaluate their cellular performance, we performed adhesion and proliferation studies using human mesenchymal stem cells (hMSCs). Cell adhesion and proliferation greatly improved for scaffolds with square and hexagonal pore geometries compared to non-porous scaffolds, recording better performance on square pores.

Acknowledgments

KS acknowledges partial financial support from George Washington University.

ORCID iDs

Mitra Aliabouzar  <https://orcid.org/0000-0002-2263-7278>

Grace Lijie Zhang  <https://orcid.org/0000-0002-3906-9692>

Kausik Sarkar  <https://orcid.org/0000-0003-0701-546X>

References

- Athanasios KA, Darling EM and Hu JC 2009 Articular cartilage tissue engineering *Synth. Lectures Tissue Eng.* **1** 1–182
- Chan B and Leong K 2008 Scaffolding in tissue engineering: general approaches and tissue-specific considerations *Eur. Spine J.* **17** 467–79
- Do A V, Khorsand B, Geary S M and Salem A K 2015 3D printing of scaffolds for tissue regeneration applications *Adv. Healthcare Mater.* **4** 1742–62
- Wüst S, Müller R and Hofmann S 2011 Controlled positioning of cells in biomaterials—approaches towards 3D tissue printing *J. Funct. Biomater.* **2** 119–54
- Zhu W, O'Brien C, O'Brien J R and Zhang L G 2014 3D nano/microfabrication techniques and nanobiomaterials for neural tissue regeneration *Nanomedicine* **9** 859–75
- O'Brien C M, Holmes B, Faucett S and Zhang L G 2014 Three-dimensional printing of nanomaterial scaffolds for complex tissue regeneration *Tissue Eng. B* **21** 103–14
- Castro N J, O'Brien J and Zhang L G 2015 Integrating biologically inspired nanomaterials and table-top stereolithography for 3D printed biomimetic osteochondral scaffolds *Nanoscale* **7** 14010–22
- Peltola S M, Melchels F P, Grijpma D W and Kellomäki M 2008 A review of rapid prototyping techniques for tissue engineering purposes *Ann. Med.* **40** 268–80
- Norman J J and Desai T A 2006 Methods for fabrication of nanoscale topography for tissue engineering scaffolds *Ann. Biomed. Eng.* **34** 89–101
- Curtis A, Casey B, Gallagher J, Pasqui D, Wood M and Wilkinson C 2001 Substratum nanotopography and the adhesion of biological cells. Are symmetry or regularity of nanotopography important? *Biophys. Chem.* **94** 275–83
- Grafahrend D et al 2011 Degradable polyester scaffolds with controlled surface chemistry combining minimal protein adsorption with specific bioactivation *Nat. Mater.* **10** 67–73
- Kohles S S et al 2012 Ultrasonic wave propagation assessment of native cartilage explants and hydrogel scaffolds for tissue engineering *Int. J. Biomed. Eng. Technol.* **10** 296–307
- Xu W and Kaufman J J 1993 Diffraction correction methods for insertion ultrasound attenuation estimation *IEEE Trans. Biomed. Eng.* **40** 563–70
- Bourbié T, Coussy O and Zinsner B 1987 *Acoustics of Porous Media* (Paris: Editions TECHNIP)
- Spirou G M, Oraevsky A A, Vitkin I A and Whelan W M 2005 Optical and acoustic properties at 1064 nm of polyvinyl chloride-plastisol for use as a tissue phantom in biomedical optoacoustics *Phys. Med. Biol.* **50** N141
- Viator J A and Prael S A 1999 Photoacoustic imaging of gelatin phantoms using matched field processing *BIOS'99 Int. Biomedical Optics Symp.* pp 276–83
- Quan K, Christison G, MacKenzie H and Hodgson P 1993 Glucose determination by a pulsed photoacoustic technique: an experimental study using a gelatin-based tissue phantom *Phys. Med. Biol.* **38** 1911
- Parker N, Mather M, Morgan S and Povey M 2010 Longitudinal acoustic properties of poly (lactic acid) and poly (lactic-co-glycolic acid) *Biomed. Mater.* **5** 055004
- Zell K, Sperl J, Vogel M, Niessner R and Haisch C 2007 Acoustical properties of selected tissue phantom materials for ultrasound imaging *Phys. Med. Biol.* **52** N475
- Prokop A F, Vaezy S, Noble M L, Kaczkowski P J, Martin R W and Crum L A 2003 Polyacrylamide gel as an acoustic coupling medium for focused ultrasound therapy *Ultrasound Med. Biol.* **29** 1351–8
- Lee K I 2011 Dependencies of the attenuation coefficient on the frequency and the trabecular thickness in trabecular-bone-mimicking phantoms: application of a scattering model
- Strelitzki R, Evans J and Clarke A 1997 The influence of porosity and pore size on the ultrasonic properties of bone investigated using a phantom material *Osteoporosis Int.* **7** 370–5
- Clarke A, Evans J, Truscott J, Milner R and Smith M 1994 A phantom for quantitative ultrasound of trabecular bone *Phys. Med. Biol.* **39** 1677
- Jeong H and Hsu D 1995 Experimental analysis of porosity-induced ultrasonic attenuation and velocity change in carbon composites *Ultrasonics* **33** 195–203
- Zhou X et al 2016 Improved human bone marrow mesenchymal stem cell osteogenesis in 3D bioprinted tissue scaffolds with low intensity pulsed ultrasound stimulation *Sci. Rep.* **6** 32876
- Aliabouzar M, Zhang L G and Sarkar K 2016 Lipid coated microbubbles and low intensity pulsed ultrasound enhance chondrogenesis of human mesenchymal stem cells in 3D printed scaffolds *Sci. Rep.* **6** 37728

- [27] Aliabouzar M, Lee S J, Zhou X, Zhang G L and Sarkar K 2018 Effects of scaffold microstructure and low intensity pulsed ultrasound on chondrogenic differentiation of human mesenchymal stem cells *Biotechnol. Bioeng.* **115** 495–506
- [28] Kassem M 2004 Mesenchymal stem cells: biological characteristics and potential clinical applications *Cloning Stem Cells* **6** 369–74
- [29] Nardi N B and da Silva Meirelles L 2008 Mesenchymal stem cells: isolation, *in vitro* expansion and characterization *Stem Cells* (Berlin: Springer) pp 249–82
- [30] Baksh D, Song L and Tuan R 2004 Adult mesenchymal stem cells: characterization, differentiation, and application in cell and gene therapy *J. Cell. Mol. Med.* **8** 301–16
- [31] Zhang C, Li J, Hu Z, Zhu F and Huang Y 2012 Correlation between the acoustic and porous cell morphology of polyurethane foam: effect of interconnected porosity *Mater. Des.* **41** 319–25
- [32] Kumar A et al 2016 Development of macroporous silicone rubber for acoustic applications *Ind. Eng. Chem. Res.* **55** 8751–60
- [33] Browne J, Ramnarine K, Watson A and Hoskins P 2003 Assessment of the acoustic properties of common tissue-mimicking test phantoms *Ultrasound Med. Biol.* **29** 1053–60
- [34] Tavakoli M and Evans J 1991 Dependence of the velocity and attenuation of ultrasound in bone on the mineral content *Phys. Med. Biol.* **36** 1529
- [35] Greenspan M and Tschiegg C E 1959 Tables of the speed of sound in water *J. Acoust. Soc. Am.* **31** 75–6
- [36] Duck F A 2013 *Physical Properties of Tissues: a Comprehensive Reference Book* (New York: Academic)
- [37] Nair S M, Hsu D K and Rose J H 1989 Porosity estimation using the frequency dependence of the ultrasonic attenuation *J. Nondestruct. Eval.* **8** 13–26
- [38] Jeong H and Hsu D 1995 Experimental analysis ultrasonic attenuation in carbon composites of porosity-induced and velocity change *J. Ultrason.* **33** 195–203
- [39] Jeong H 1997 Effects of voids on the mechanical strength and ultrasonic attenuation of laminated composites *J. Compos. Mater.* **31** 276–92
- [40] Chaffai S, Padilla F, Berger G and Laugier P 2000 *In vitro* measurement of the frequency-dependent attenuation in cancellous bone between 0.2 and 2 MHz *J. Acoust. Soc. Am.* **108** 1281–9
- [41] Madsen E L, Frank G R and Dong F 1998 Liquid or solid ultrasonically tissue-mimicking materials with very low scatter *Ultrasound Med. Biol.* **24** 535–42
- [42] Madsen E L, Zagzebski J A, Banjavie R A and Jutila R E 1978 Tissue mimicking materials for ultrasound phantoms *Med. Phys.* **5** 391–4
- [43] Dussik K T, Fritch D J, Kyriazidou M and Sear R S 1958 Measurements of articular tissues with ultrasound *Am. J. Phys. Med. Rehabil.* **37** 160–5
- [44] Agemura D H, O'Brien W D Jr, Olerud J E, Chun L E and Eyre D E 1990 Ultrasonic propagation properties of articular cartilage at 100 MHz *J. Acoust. Soc. Am.* **87** 1786–91
- [45] Johnston R et al 1979 *Elements of tissue characterization Ultrasonic Tissue Characterization II* (Washington: Spec. Publishers) pp 19–27
- [46] Demitri C, Sannino A, Conversano F, Casciaro S, Distante A and Maffezzoli A 2008 Hydrogel based tissue mimicking phantom for *in-vitro* ultrasound contrast agents studies *J. Biomed. Mater. Res. B* **87** 338–45
- [47] Povey M J 1997 *Ultrasonic Techniques for Fluids Characterization* (New York: Academic)
- [48] De Santis R et al 2015 Towards the design of 3D fiber-deposited poly(-caprolactone)/iron-doped hydroxyapatite nanocomposite magnetic scaffolds for bone regeneration *J. Biomed. Nanotechnol.* **11** 1236–46
- [49] Hunger P M, Donius A E and Wegst U G 2013 Structure–property–processing correlations in freeze–cast composite scaffolds *Acta Biomater.* **9** 6338–48
- [50] Banavar J R, Koplik J and Winkler K W 1987 *Physics and Chemistry of Porous Media II* (Ridgefield, CT, 1986) (American Institute of Physics)
- [51] De Santis R, D'Amora U, Russo T, Ronca A, Gloria A and Ambrosio L 2015 3D fibre deposition and stereolithography techniques for the design of multifunctional nanocomposite magnetic scaffolds *J. Mater. Sci., Mater. Med.* **26** 250
- [52] Loh Q L and Choong C 2013 Three-dimensional scaffolds for tissue engineering applications: role of porosity and pore size *Tissue Eng. B* **19** 485–502
- [53] Knychala J, Bouropoulos N, Catt C, Katsamenis O, Please C and Sengers B 2013 Pore geometry regulates early stage human bone marrow cell tissue formation and organisation *Ann. Biomed. Eng.* **41** 917–30
- [54] Rumpler M, Woesz A, Dunlop J W, van Dongen J T and Fratzl P 2008 The effect of geometry on three-dimensional tissue growth *J. R. Soc. Interface* **5** 1173–80
- [55] Jin Q, Takita H, Kohgo T, Atsumi K, Itoh H and Kuboki Y 2000 Effects of geometry of hydroxyapatite as a cell substratum in BMP-induced ectopic bone formation *J. Biomed. Mater. Res.* **51** 491–9
- [56] Habibovic P, Yuan H, van der Valk C M, Meijer G, van Blitterswijk C A and de Groot K 2005 3D microenvironment as essential element for osteoinduction by biomaterials *Biomaterials* **26** 3565–75
- [57] Nelson C M et al 2005 Emergent patterns of growth controlled by multicellular form and mechanics *Proc. Natl Acad. Sci. USA* **102** 11594–9